Bright and stable perovskite light-emitting diodes in the near-infrared range

Yuqi Sun[1]†, Lishuang Ge[2]†, Linjie Dai[1], Changsoon Cho[1], Jordi Ferrer Orri[1,3,4], Kangyu Ji[1], Szymon J. Zelewski[1,5], Yun Liu[1,6], Alessandro J. Mirabelli[1,3], Youcheng Zhang[1], Jun-Yu Huang[1], Yusong Wang[7], Ke Gong[7], May Ching Lai[4], Lu Zhang[1], Dan Yang[2], Jiudong Lin[2], Elizabeth M. Tennyson[1], Caterina Ducati[4], Samuel D. Stranks[1,3], Lin-Song Cui[2]*, Neil C. Greenham[1]*

[1] *Cavendish Laboratory, University of Cambridge, J. J. Thomson Avenue, Cambridge CB3 0HE, UK.*

[2] *CAS Key Laboratory of Soft Matter Chemistry, Department of Polymer Science and Engineering, University of Science and Technology of China, Hefei 230026, Anhui, China.*

[3] *Department of Chemical Engineering and Biotechnology, University of Cambridge, Philippa Fawcett Avenue, Cambridge CB3 0AS, UK.*

[4] *Department of Materials Science, University of Cambridge, 27 Charles Babbage Rd, Cambridge CB3 0FS, UK.*

[5] *Department of Semiconductor Materials Engineering, Faculty of Fundamental Problems of Technology, Wrocław University of Science and Technology, Wybrzeże Wyspiańskiego 27, 50-370, Wrocław, Poland.*

[6] *Institute of High Performance Computing, Agency for Science Technology and Research, 1 Fusionopolis Way, Singapore 138632.*

[7] *Hefei National Research Centre for Physical Sciences at the Microscale, University of Science and Technology of China, Hefei 230026, Anhui, China.*

†These authors contributed equally

**Emails: Lin-Song Cui (lscui@ustc.edu.cn), Neil C. Greenham (ncg11@cam.ac.uk)*

Abstract

Perovskite light-emitting diodes (LEDs) have attracted broad attention due to their rapidly increasing external quantum efficiencies (EQEs) [1–15]. However, most high EQEs of perovskite LEDs are reported at low current densities (< 1 mA cm^{-2}) and low brightness. Decrease in efficiency and rapid degradation at high brightness inhibit their practical applications. Here, we demonstrate perovskite LEDs with exceptional performance at high brightness, achieved by the introduction of a multifunctional molecule that simultaneously removes non-radiative regions in the perovskite films and suppresses luminescence quenching of perovskites at the interface with charge-transport layers. The resulting LEDs emit near-infrared light at 800 nanometres, exhibit a peak EQE of 23.8 % at 33 mA cm^{-2} and retain EQEs over 10 % at high current densities of up to 1,000 mA cm^{-2}. In pulsed operation, they retain EQE of 16 % at an ultra-high current density of 4,000 mA cm^{-2}, along with a high radiance of over 3,200 W s^{-1} m^{-2}. Notably, an operational half-lifetime of 32 hours at an initial radiance of 107 W s^{-1} m^{-2} has been achieved, representing the best stability for perovskite LEDs having EQEs exceeding 20% at high brightness levels. The demonstration of efficient and stable perovskite LEDs at high brightness is an important step toward commercialisation and opens up new opportunities beyond conventional LED technologies, such as perovskite electrically pumped lasers.

Main

Solution-processable metal halide perovskites exhibit luminescence with high colour purity, tuneable emission wavelengths and excellent charge-transport properties. They have been considered as potential candidates for high-performance light-emitting diodes (LEDs)[1–15] with low cost, flexibility and light weight. In the past decade, perovskite LEDs have been extensively optimised, often by incorporation of molecular additives[5–9], and external quantum efficiencies (EQEs) of over 20 % have been achieved[5–9]. The emergence of more efficient perovskite LEDs continues, along with improved stability at low brightness. However, high EQEs and improved stability were mostly reported at low current densities and brightness. Retaining EQE and stability at high brightness is already the key challenge for commercialisation of perovskite LEDs.

In this work, we design a multifunctional molecule 2-[4-(methylsulfonyl)phenyl]ethylamine (MSPE, **Fig. 1a**) to manipulate the optoelectronic, crystal and morphological properties of 3D cubic phase (α-phase) formamidinium (FA) lead triiodide ($FAPbI_3$) perovskites and demonstrate efficient and operationally stable near-infrared (NIR) perovskite LEDs at high brightness. MSPE improves crystallinity and photoluminescence efficiency and induces homogenous emission by removing non-radiative dark regions in the perovskite films. As a multifunctional additive, MSPE also provides a barrier to quenching of perovskite luminescence at the interface with charge-transport layers. In addition, MSPE devices show reduced Joule heating, which allows high EQE to be maintained at ultra-high current densities and reduces thermal degradation.

We fabricated $FAPbI_3$-based perovskite LEDs with the device architecture as follows: glass/ indium tin oxide (ITO, 150 nm)/ zinc oxide (ZnO, 35 nm)/ ethoxylated polyethylenimine (PEIE, ~ 0.5 nm)/ perovskite ($FAPbI_3$, 30 nm)/ poly(4-butylphenyl-diphenylamine) (poly-TPD, 40 nm)/ molybdenum oxide (MoO_x, 7 nm)/ gold (Au, 60 nm) (**Fig. 1b**). ITO and Au function as electrodes. ZnO and poly-TPD serve as electron- and hole-transport layers, respectively. A thin PEIE layer is used to improve the wettability of ZnO. MoO_x acts as the hole-injection layer. The $FAPbI_3$ perovskites were prepared via spin-coating from FAI, PbI_2 and MSPE precursors at a molar ratio of 2.7: 1: x (x = 0 – 0.9). The device performance is dependent on the molar fraction of MSPE relative to PbI_2 (**Fig. 1d**, Supplementary Fig. 1). As a 0.5 molar fraction of

MSPE/PbI_2 exhibits the best device performance, the films and devices with this composition are hereafter referred to as "MSPE". The samples without MSPE are referred to as "control". The angle-dependent electroluminescence (EL) intensity of MSPE-based LEDs follows a Lambertian profile (**Fig. 1c**). The current density–voltage–radiance (*J–V–R*) characteristic of a champion MSPE LED is shown in **Fig. 1e**. The current density and radiance of MSPE LEDs rise rapidly after 1.3 V, which is lower than the bandgap voltage of $FAPbI_3$ (1.55 eV) and indicates efficient charge transport and injection[16,17]. Their EL peaks at 800 nm with a narrow full-width at half-maximum of 39 nm and has a stable shape under bias (**Fig. 1f**). The champion MSPE-based devices have a peak EQE of 23.8 % at a high radiance of 39 W sr^{-1} m^{-2} (**Fig. 1e, f**). The brightness rises quickly with voltage and yields 497 W sr^{-1} m^{-2} (photon flux of 6.3 × 10^{21} m^{-2} s^{-1}) at 4.4 V. It is noteworthy that an EQE of over 10 % is retained at high current densities of up to 1,000 mA cm^{-2}. The maximum radiance achieved is 663 W sr^{-1} m^{-2} in another device with a peak EQE of 22.2 %. Note that radiance is used to evaluate brightness of NIR LEDs, as luminance only applies to visible light (Supplementary Note 1)[18]. These NIR emitters are attractive for a wide variety of applications such as imaging[19], optogenetics[20], night-vision[21], communication[22] and lasing[23,24]. To the best of our knowledge, in the NIR regime, this combination of high EQE and high radiance found in MSPE-based LEDs is superior to previously reported perovskite, organic, and quantum-dot LEDs (**Fig. 1g**).

MSPE devices exhibit high energy conversion efficiency (ECE) of up to 16 % (Supplementary Fig. 2). This implies reduction of the electrical power and Joule heating to drive the devices, allowing EQE to be maintained at high brightness and prolonging the device lifetime. MSPE-based LEDs show a rapid increase in radiance and a smaller increase in device temperature during the voltage scan compared to control ones (Supplementary Fig. 3). To relieve Joule heating, pulsed voltages have been applied to devices, which enables sufficient time for heat dissipation. As a result, MSPE devices achieve EQE of 16 % at an ultrahigh current density of 4,000 mA cm^{-2}, along with a high radiance of over 3,200 W sr^{-1} m^{-2}.

Furthermore, MSPE-based LEDs show reasonable reproducibility. We fabricated 42 devices with the same procedures and their peak EQE and radiance histograms are shown in **Fig. 1h**. The histograms show a mean EQE of 20 % with a standard deviation of 1.6 % and a mean peak radiance of nearly 500 W sr^{-1} m^{-2}. MSPE LEDs with a simple glass-epoxy encapsulation exhibit a half-lifetime (T_{50}, the time to reach 50 % of the initial brightness) of 32 hours for a very high initial radiance of 107 W sr^{-1} m^{-2} at a constant current density of 100 mA cm^{-2} (**Fig.**

1i). EL spectra and voltages were stable during lifetime measurement (Supplementary Fig. 4-5). The control devices show poor T_{50} of 5 hours for an initial radiance of ~ 10 W sr^{-1} m^{-2} (Supplementary Fig. 6). MSPE LEDs represent the best stability for perovskite LEDs having EQE exceeding 20 % at high brightness levels (Supplementary Fig. 4; Supplementary Table. 1-2). To predict lifetimes at lower radiance, we fitted measured lifetimes at various initial radiances with an empirical formula [15,25]. For an initial radiance of 5 W sr^{-1} m^{-2}, T_{50} of MSPE devices is estimated to be 5×10^4 hours (Supplementary Fig. 4), comparable to the state-of-the-art organic and quantum-dot LEDs (Supplementary Table. 3).

To understand the underlying reasons for the improved performance of MSPE-based devices, we performed film characterisations as follows. Grazing-incidence wide-angle X-ray scattering (GIWAXS) measurements show that both films exhibit typical α-phase scattering characteristics at around 1 $Å^{-1}$ (**Fig. 2a**). The scattering characteristics of the control film are isotropic, indicating that perovskite crystallites are randomly oriented[26]. MSPE induces an oriented crystallization as GIWAXS shows a preferential orientation of perovskites along the surface normal direction[27,28]. X-ray diffraction (XRD) analysis shows the sharp and strong peaks of α-phase $FAPbI_3$ in the MSPE film, indicating vastly improved crystallinity compared to the control film (**Fig. 2d**)[29]. Hyperspectral microscopy further unveils the heterogeneities of PL peak wavelength across the control films (**Fig. 2b**), indicating disorder of local energetic structure. MSPE significantly mitigates this disorder, leading to uniform peak wavelength in the films (**Fig. 2b**). Crystallographic and energetic disorder provides non-radiative recombination centres undermining device performance[26,30], which are mitigated by MSPE. Consequently, MSPE films show improved PLQEs over a wide range of excitation intensity (**Fig. 2e**). Their PLQEs remain over 40 % even at a low excitation intensity of 0.02 mW cm^{-2}, indicating reduced defect-mediated non-radiative recombination in MSPE films. Reduction of defect-mediated recombination is also confirmed by time-resolved PL spectroscopy as MSPE shows slower PL decay (Supplementary Fig. 7).

Nanoscopic morphology and emission properties of these films are further investigated. From scanning electron microscopy (SEM, **Fig. 2c**), irregular and discontinuous perovskite polycrystalline grains are distributed on top of ZnO substrate in the control samples. Perovskite grains in MSPE films are denser and adopt a regular island shape. Atomic force microscopy (AFM, Supplementary Fig. 8) shows similar morphology to SEM. From AFM, the root mean

square surface roughness reduces from 13.7 nm to 3.6 nm with the addition of MSPE, which could be attributed to a thin organic layer filling in the gaps between perovskite grains[5]. Then cathodoluminescence (CL) signals from SEM visualise the emission profile of these grains (**Fig. 2c**). MSPE films have mean CL intensity of 11.7 counts, more than twice stronger than that of the control ones (4.8 counts) under the same acquisition conditions. Strong CL intensity indicates that luminescence efficiency is promoted with MSPE (Supplementary Note 2). MSPE also slows down the degradation of perovskites under electron beam exposure (Supplementary Fig. 9). These observations confirm that MSPE reduces non-radiative recombination in the perovskite grains, consistent with the PL measurements.

The improved quality of perovskite films is attributed to MSPE, the roles of which are further unveiled by Fourier-transform infrared spectroscopy (FTIR), X-ray photoelectron spectroscopy (XPS), nuclear magnetic resonance (NMR) and density functional theory (DFT) simulations. FTIR reveals that the amino group scissoring vibration $\delta(NH_2)$ of MSPE at around 1646 cm^{-1} is significantly broadened and nearly invisible in the MSPE + FAI sample (**Fig. 2f**), indicating that the N-H chemical bond is greatly weakened by the addition of FAI. Consistent with this, ^{127}I NMR spectrum of FAI is significantly broadened with the addition of MSPE (**Fig. 2g**). Strong interaction with FAI could slow down the growth of perovskites during film formation, contributing to high crystallinity and regular shape of grains (Supplementary Note 3; Supplementary Fig. 16-18). The sulfonyl group can interact with FAI or PbI_2 as the stretching vibration ν(S=O) is broadened and shifts to lower wavenumbers in both mixture samples (**Fig. 2f**). XPS further unveils that the Pb 4*f* signals of PbI_2 shift to lower binding energies with MSPE (**Fig. 2h**), while the O 1*s* signal of MSPE shifts to higher binding energy (Supplementary Fig. 10), indicating that the oxygen atoms in the sulfonyl group can donate their lone electron pairs to the empty 6*p* orbital of Pb atoms[8]. This suggests that unsaturated Pb dangling bonds due to halide vacancy can be passivated by MSPE. DFT simulations reveal trap-free bandgap of perovskites with MSPE passivation and further show that both amino group and sulfonyl group can bind with perovskites (Supplementary Fig. 11).

MSPE can also interact with other MSPE molecules through hydrogen bonding. FTIR measurements of MSPE molecules with different concentrations were performed. Both $\delta(NH_2)$ and ν(S=O) signals are broadened as the concentration of MSPE increases (**Fig. 2i**), suggesting hydrogen bonding interactions between the amino group and the sulfonyl group of

MSPE (N-H···O=S). Hydrogen bonding between two functional groups is further examined by using methyl phenyl sulfone (MPS, with a sulfonyl group) and phenethylamine (PEA, with an amino group) (Supplementary Fig. 12). The addition of MPS causes upfield-shifting of ^{1}H NMR signals of the amino group in PEA, indicating increasing electron density due to hydrogen bonding (N-H···O=S). Consistent with this, FTIR also suggests that both the sulfonyl group of MPS and the amino group of PEA are broadened in the mixture sample (Supplementary Fig. 12).

The above investigations reveal the roles of the multifunctional molecule MSPE. MSPE induces high crystallinity and reduces various defects in perovskite films, leading to improved PLQE and reduced crystallographic and energetic disorder (**Fig. 2a-e**). Charge-carrier kinetics further confirm the reduction of defects and disorder in MSPE films (**Fig. 3**). In addition, MSPE can assemble in between perovskite grains through hydrogen bonding and form a physical spacer between charge-transport layers, removing interfacial quenching pathways (**Fig. 4**).

Confocal PL microscopy shows that the control films have significant spatial variation in PL intensity on the lengthscale of micrometres (**Fig. 3a**). The dark regions in the control samples correlate with reduced PL lifetime, indicating that these dark regions contain a higher concentration of defects serving as non-radiative centres[31,32]. In contrast, the MSPE films show much more homogenous intensity and a uniformly long lifetime on the same lengthscale (**Fig. 3c**). The absence of defect-containing dark regions in MSPE films is consistent with the improved overall PLQE and carrier lifetime relative to the control films. Quantitative analysis of the recombination process by transient absorption measurements was performed to evaluate the defect concentration of perovskite films (Supplementary Fig. 13). The defect-mediated non-radiative recombination (k_1), bimolecular recombination (k_2), and Auger recombination (k_3) rate constants are extracted from the rate equation for charge carrier population (Supplementary Note 4). As shown in **Fig. 3b** and **d**, k_1 of MSPE films (6.2×10^6 s^{-1}) is nearly an order of magnitude lower than that of the control films (4.2×10^7 s^{-1}), indicating a significant decrease of defect density with the introduction of MSPE molecules. Photothermal deflection spectroscopy (PDS) also reveals reduced defect concentrations in MSPE films (Supplementary Fig. 14)[33].

Another function of the MSPE additive is to prevent luminescence quenching of perovskites at the charge-transport interfaces. In the control devices, since perovskite grains are discontinuous on ZnO (**Fig. 2c**, Supplementary Fig. 1), poly-TPD on top of perovskites can directly contact with ZnO as demonstrated in **Fig. 4a**. PDS shows that the ZnO + poly-TPD mixture sample forms interfacial states with energies lower than the bandgap of $FAPbI_3$ (Supplementary Fig. 15), which can quench the emission of perovskites and serve as non-radiative loss channels undermining device performance. To investigate interfacial quenching, the PL decay kinetics of perovskites in multilayer systems were measured by selectively exciting the perovskites with a 560 nm laser where charge-transport materials have negligible absorption. As shown in **Fig. 4b**, the PL decays faster when poly-TPD or TFB is present on top of perovskite samples. We propose that the luminescence quenching is caused by energy transfer from the perovskite to low-energy states with charge-transfer character at the ZnO/poly-TPD (or TFB) interface. With PVK or TPBi, no quenching is observed since their deeper highest occupied molecular orbital levels raise the energy of the interfacial states above the perovskite bandgap (**Fig. 4c**). MSPE can assemble between discontinuous perovskite grains as discussed above and provide a physical spacer between ZnO and the hole-transport materials (**Fig. 4d**). As a result, none of the hole-transport layers causes observable quenching of MSPE perovskites (**Fig. 4e, f**). The existence of the spacer is further characterised as follows. SEM images of high magnification (Supplementary Fig. 1) show that ZnO between perovskite grains in MSPE-based film is covered by dark regions composed of organics with lower atomic numbers (Supplementary Note 5). Increasing molar ratio of MSPE leads to increasing areal density of dark regions and decreasing areal density of the perovskite grains, suggesting that the dark regions are MSPE. The existence of the organic spacer in MSPE films is also consistent with AFM measurements (Supplementary Fig. 8) as discussed before. A cross-section STEM-HAADF image of a half device sample with a structure of ZnO/PEIE/MSPE-based perovskite/Au and associated energy-dispersive X-ray spectroscopy (Supplementary Fig. 19) show that an organic layer of MSPE fills the gaps between perovskite grains.

In this work, a multifunctional molecule MSPE was designed to control the optoelectronic, crystal and morphological properties of perovskite films. MSPE improves crystallinity and removes non-radiative dark regions in the perovskite films. Simultaneously, self-assembly of MSPE between discontinuous perovskite grains removes interfacial quenching pathways in the devices. Comprehensive suppression of non-radiative pathways in the films and devices allows us to achieve efficient and bright perovskite LEDs with the best operating stability among

perovskite LEDs having EQE exceeding 20 % at high brightness. Our results suggest that low-temperature solution-processable perovskite LEDs have the potential to achieve high efficiency at high brightness and to surpass conventional LED technologies.

References

1. Tan, Z.-K. *et al.* Bright light-emitting diodes based on organometal halide perovskite. *Nat. Nanotechnol.* **9**, 687–692 (2014).

2. Hassan, Y. *et al.* Ligand-engineered bandgap stability in mixed-halide perovskite LEDs. *Nature* **591**, 72–77 (2021).

3. Zhao, B. *et al.* High-efficiency perovskite–polymer bulk heterostructure light-emitting diodes. *Nat. Photon.* **12**, 783–789 (2018).

4. Kim, Y.-H. *et al.* Comprehensive defect suppression in perovskite nanocrystals for high-efficiency light-emitting diodes. *Nat. Photon.* **15**, 148–155 (2021).

5. Cao, Y. *et al.* Perovskite light-emitting diodes based on spontaneously formed submicrometre-scale structures. *Nature* **562**, 249–253 (2018).

6. Xu, W. *et al.* Rational molecular passivation for high-performance perovskite light-emitting diodes. *Nat. Photon.* **13**, 418–424 (2019).

7. Zhao, B. *et al.* Efficient light-emitting diodes from mixed-dimensional perovskites on a fluoride interface. *Nat. Electron.* **3**, 704–710 (2020).

8. Ma, D. *et al.* Distribution control enables efficient reduced-dimensional perovskite LEDs. *Nature* **599**, 594–598 (2021).

9. Guo, B. *et al.* Ultrastable near-infrared perovskite light-emitting diodes. *Nat. Photon.* **16**, 637–643 (2022).

10. Chiba, T. *et al.* Anion-exchange red perovskite quantum dots with ammonium iodine salts for highly efficient light-emitting devices. *Nat. Photon.* **12**, 681–687 (2018).

11. Chu, Z. *et al.* Perovskite light-emitting diodes with external quantum efficiency exceeding 22% via small-molecule passivation. *Adv. Mater.* **33**, 2007169 (2021).

12. Xiao, Z. *et al.* Efficient perovskite light-emitting diodes featuring nanometre-sized crystallites. *Nat. Photon.* **11**, 108–115 (2017).

13. Chen, J. *et al.* Efficient and bright white light-emitting diodes based on single-layer heterophase halide perovskites. *Nat. Photon.* **15**, 238–244 (2021).

14. Kim, J. S. *et al.* Ultra-bright, efficient and stable perovskite light-emitting diodes. *Nature* **611**, 688–694 (2022).

15. Lin, K. *et al.* Perovskite light-emitting diodes with external quantum efficiency exceeding 20 per cent. *Nature* **562**, 245–248 (2018).

16. Lian, Y. *et al.* Ultralow-voltage operation of light-emitting diodes. *Nat. Commun.* **13**, 3845 (2022).

17. Santhanam, P., Gray, D. J. & Ram, R. J. Thermoelectrically pumped light-emitting diodes operating above unity efficiency. *Phys. Rev. Lett.* **108**, 097403 (2012).

18. Anaya, M. *et al.* Best practices for measuring emerging light-emitting diode technologies. *Nat. Photon.* **13**, 818–821 (2019).

19. Michalet, X. *et al.* Quantum qots for live cells, in vivo imaging, and diagnostics. *Science* **307**, 538–544 (2005).

20. Chen, S. *et al.* Near-infrared deep brain stimulation via upconversion nanoparticle–mediated optogenetics. *Science* **359**, 679–684 (2018).

21. Pan, Z., Lu, Y.-Y. & Liu, F. Sunlight-activated long-persistent luminescence in the near-infrared from Cr^{3+}-doped zinc gallogermanates. *Nat. Mater.* **11**, 58–63 (2012).

22. Bao, C. *et al.* Bidirectional optical signal transmission between two identical devices using perovskite diodes. *Nat. Electron.* **3**, 156–164 (2020).

23. Deschler, F. *et al.* High photoluminescence efficiency and optically pumped lasing in solution-processed mixed halide perovskite semiconductors. *J. Phys. Chem. Lett.* **5**, 1421–1426 (2014).

24. Zhao, L. *et al.* Nanosecond-pulsed perovskite light-emitting diodes at high current density. *Adv. Mater.* **33**, 2104867 (2021).

25. Dai, X. *et al.* Solution-processed, high-performance light-emitting diodes based on quantum dots. *Nature* **515**, 96–99 (2014).

26. Jariwala, S. *et al.* Local crystal misorientation influences non-radiative recombination in halide perovskites. *Joule* **3**, 3048–3060 (2019).

27. Min, H. *et al.* Efficient, stable solar cells by using inherent bandgap of α-phase formamidinium lead iodide. *Science* **366**, 749–753 (2019).

28. Kim, G. *et al.* Impact of strain relaxation on performance of α-formamidinium lead iodide perovskite solar cells. *Science* **370**, 108–112 (2020).

29. Han, Q. *et al.* Single crystal formamidinium lead Iodide ($FAPbI_3$): insight into the structural, optical, and electrical properties. *Adv. Mater.* **28**, 2253–2258 (2016).

30. Doherty, T. A. S. *et al.* Performance-limiting nanoscale trap clusters at grain junctions in halide perovskites. *Nature* **580**, 360–366 (2020).

31. Quilettes, D. W. de *et al.* Impact of microstructure on local carrier lifetime in perovskite solar cells. *Science* **348**, 683–686 (2015).

32. Draguta, S. *et al.* Spatially non-uniform trap state densities in solution-processed hybrid perovskite thin films. *J. Phys. Chem. Lett.* **7**, 715–721 (2016).

33. Zhang, W. *et al.* Ultrasmooth organic–inorganic perovskite thin-film formation and crystallization for efficient planar heterojunction solar cells. *Nat. Commun.* **6**, 6142 (2015).

34. Orri, J. F. *et al.* Using Cathodoluminescence from Continuous and Pulsed-Mode SEM to Elucidate the Nanostructure of Hybrid Halide Perovskite Materials. *Microsc. Microanal.* **28**, 2006–2008 (2022).

Fig. 1: Perovskite LED structure and performance.

a, Molecular structure of MSPE. **b**, STEM- HAADF image of a full MSPE LED. Scale bar: 200 nm. **c**, Ideal Lambertian profile and experimental angle-dependent emission data. **d**, Peak EQE distribution of devices fabricated from precursors with different molar fractions of MSPE/PbI_2. **e**, Current density versus voltage (black) and radiance versus voltage (red) characteristics of the champion MSPE LED. **f**, EQE versus current density characteristics of the champion device. Inset shows their EL spectra at different bias. **g**, Reported peak EQE and peak radiance of various NIR LEDs according to the data provided in Supplementary Table 1, 3. **h**, Peak EQE (left) and peak radiance (right) histograms of 42 MSPE LEDs. **i**, Operational stability measurement.

Fig. 2: Characteristics of perovskite films and molecular interactions.

a, GIWAXS patterns of perovskite films. **b**, Hyperspectral image of perovskite films. Scale bar: 10 μm. **c**, SEM image at 5 kV (left) and the corresponding CL intensity map (right) of the control and MSPE films. Scale bar: 400 nm. © Cambridge University Press; Reproduced with permission from [34], © Microscopy Society of America 2022, published by Cambridge University Press. **d**, XRD patterns of perovskite films. **e**, PLQE of perovskite films. **f,** FTIR spectra of MSPE and perovskite precursors. **g**, ^{127}I NMR spectra. **h,** XPS spectra of Pb 4*f*. **i**, FTIR spectra of MSPE molecules of different concentrations.

Fig. 3: Charge-carrier kinetics of perovskite films.

a, Confocal PL intensity (left) and lifetime (right) of the control films and **c** of MSPE films. Scale bar: 5 μm. **b**, Recombination rate $dn(t)/dt$ against charge carrier density $n(t)$ of control films and **d** of MSPE films.

Fig. 4: Time-resolved photoluminescence decay kinetics of perovskites with charge-transport layers.

a, Schematic illustration of the control perovskite grains with charge-transport layers in a full device and **d** of the MSPE-based perovskite grains. **b-c**, Time-resolved photoluminescence decay kinetics of ZnO/PEIE/Control samples coated with different hole-transport materials and **e-f** of MSPE samples.

Acknowledgements

Y. S. and L.D. acknowledge support from the China Scholarship Council and Cambridge Trust Scholarship. L. G., L.C. and D.Y. acknowledge funding from the USTC Research Funds of the Double First-Class Initiative and the National Natural Science Foundation of China (NSFC) (52103242). This work was partially carried out at the USTC Centre for Micro and Nanoscale Research and Fabrication. This work used resources of the supercomputing system in the Supercomputing Centre of University of Science and Technology of China. C.C. and S.D.S. acknowledge the BrainLink program funded by the Ministry of Science and ICT through the National Research Foundation of Korea (NRF-2022H1D3A3A01077343). J. F. O acknowledges funding from the Engineering and Physical Sciences Research Council (EPSRC) Nano Doctoral Training Centre (EP/L015978/1). SEM-CL studies were supported by the EPSRC (EP/R025193/1) and Dr Gunnar Kusch is thanked for his ongoing support with the CL system. K. J. acknowledges funding from the Royal Society. S. D. S. acknowledges funding from the Royal Society and Tata Group (UF150033). The authors acknowledge support from the European Research Council (ERC, European Union's Horizon 2020, HYPERION 756962 and PEROVSCI 957513). S. J. Z. acknowledges support from the Polish National Agency for Academic Exchange within the Bekker program (PPN/BEK/2020/1/00264/U/00001). Y. L. acknowledges support from Simons Foundation (601946). This work used resources provided by the Cambridge Service for Data Driven Discovery (CSD3) operated by the University of Cambridge Research Computing Service, provided by Dell EMC and Intel using Tier-2 funding from the EPSRC (EP/P020259/1), and DiRAC funding from the Science and Technology Facilities Council. GIWAXS studies were supported by Diamond Light Source for time on Beamline I07 under proposal numbers SI30575-1 and SI30043-1 and Dr Miguel Anaya, Dr Yang Lu, Yu-Hsien Chiang and Qichun Gu helped with measurement. This work was supported by EPSRC grants EP/R023980/1, EP/S030638/1 and EP/V06164X/1.

Author contributions

Y. S., L. C., and N. C. G. conceived the work. Y. S. developed efficient perovskite LEDs under the supervision of L.C. and N. C. G. L. G. performed chemical synthesis, FTIR and XPS under the supervision of L. C. L. D. performed TA measurements. Y. S. and L. D. performed time-resolved PL measurements. C. C. performed confocal TCSPC measurements. J. F. O and M. L. performed STEM-HAADF and EDS measurements under the supervision of C. D. J. F. O performed SEM-CL measurements. K. J. performed hyperspectral imaging measurements. S. J. Z. performed PDS measurements. A. J. M. performed GIWAXS measurements. Y. L. performed DFT simulations. Y. Z. performed SEM measurements. L. G., Y. W., K. G., and D. Y. performed NMR measurements. L. Z. performed AFM measurements. J. H., J. L., E. M. T and S. D. S. assisted in interpreting results. Y. S. wrote the manuscript, which was revised by L. C. and N. C. G. All authors contributed to the work and commented on the paper.

Methods

Materials

All chemicals were purchased from Sigma Aldrich, unless otherwise stated. The perovskite precursor solution was prepared by dissolving FAI (Greatcell Solar Materials), PbI_2 (Alfa Aesar) and MSPE at a molar ratio of 2.7: 1: x (x = 0 - 0.9) in *N*,*N*-dimethylformamide (DMF) to give an overall concentration of 7 wt%. Poly-TPD was purchased from 1-Materials. ZnO nanoparticles were synthesised according to previously reported procedures[35]. MSPE was purchased from Fluorochem or synthesized and purified according to the method in previous literature[36] with modifications described as follows. In a two-neck flask, 4-(methylsulfonyl)phenylacetonitrile (3.9 g, 20 mmol, J&K Chemical) was dissolved in 30 mL dehydrated THF under nitrogen atmosphere. The mixture was cooled to 0 °C for 10 minutes. Then lithium aluminium hydride solution in THF (2.4 M, 8.3 mL, 20 mmol) was added drop by drop in 10 minutes. After stirring under nitrogen for an hour, the reaction mixture was carefully quenched by excess sodium sulfate decahydrate. The product was extracted with ethyl acetate, and the combined organic layer was dried over anhydrous sodium sulfate. After filtration and evaporation, the crude product was purified by column chromatography on silica gel (eluent: hexane/ ethyl acetate = 7:3, v/v) and recrystallization from chloroform/methanol to afford MSPE as solid (1.52 g, yield: 38%, purity: 99.5%). ^{1}H NMR (400 MHz, DMF-d7): δ 8.08 (d, J = 8.0 Hz, 2H), 7.73 (d, J = 8.0 Hz, 2H), 3.42 (s, 3H), 3.10 (m, 2H), 2.93 (m, 2H).

PeLED fabrication and characterisations

Pre-patterned ITO-coated glass substrates (10-15 Ω sq^{-1}, Kintec) were cleaned by ultrasonic bath in detergent, water, acetone and isopropanol for 5 min, consecutively. Then the ITO substrates were dried and treated by oxygen plasma etching (forward power 200 W, reflected power 0 W, 10 min). ZnO nanoparticles were spin-coated on ITO substrates at 3000 RPM and then annealed at 150 °C for 10 min. Subsequently, 0.45 wt% PEIE in 2-methoxyethanol solution was spin-coated at 5000 RPM and annealed 100 °C for 15 min. The substrates were transferred into a nitrogen-filled glovebox. The perovskite layer was deposited by spin-coating precursor solution on ZnO/PEIE substrates at 3000 RPM for 60 s and then annealing at 100°C for 10 min. On top of the perovskite layer, poly-TPD (14 mg ml^{-1} in chlorobenzene) was spin-coated at 3000 RPM for 40 s. Finally, 7 nm of MoO_x and 60 nm of gold were sequentially evaporated as top electrodes through a shadow mask (active device area 4.5 mm^2) at a pressure of 5×10^{-6} mbar. All devices were encapsulated by epoxy with a glass cover for further

measurements. *J–V–R* characteristics were measured using a Keithley 2400 source-measure unit and a calibrated silicon photodetector. The detailed methods have been published in a previous article[18]. In short, an LED was connected with a Keithley 2400 source-measure unit and the photodetector was placed on-axis in front of the LED. The current that flowed through the LED was measured at a given voltage from zero bias to forward bias. Simultaneously, the signal generated in the photodetector by the photons emitted by the LED was measured. The LED metrics were calculated taking into account the responsivity of the photodetector, the geometry of the setup and the EL spectrum. This measurement setup was previously cross-checked independently with a third-party industrial laboratory and other research groups[5,37-38]. EL spectra were measured by an Andor iDus spectrograph with a Si array detector. Device temperature and infrared images were recorded by Hti HT-H8 thermal imaging camera. For operational lifetime measurement, an LED with glass-epoxy encapsulation was connected with a Keithley 2400 source-measure unit, which provided a constant current, in ambient environment at room temperature. A photodetector was used to collect the emitted photons from the LED. At the beginning and the end of the measurement, the emission spectra were measured by a spectrometer (Ocean Insight).

STEM-HAADF

Cross-sectional lamellae were cut and thinned to electron transparency (200 nm) using a FEI Helios Nanolab Dualbeam FIB/SEM following a standard protocol. The lamellae were directly transferred to a FEI Osiris TEM operated at 200 kV, minimising air exposure to less than 2 min. To minimise beam damage, high-angle annular dark field images (STEM-HAADF) were acquired using at a beam current of around 140 pA, dwell time of 30 ms / pixel, camera length of 115 mm, and spatial sampling of 5 nm / pixel.

Film characterisations

A combination of 520 nm continuous-wave laser, an integrating sphere and an Andor iDus Si detector was used to measure the steady-state PL and PLQEs[39]. The excitation intensity was tuned by a filter with a focused beam spot of ~ 0.3 mm^2. XRD data was collected by X-Ray Bruker D8 under an ambient environment. Hyperspectral images of photoluminescence were measured using a wide-field hyperspectral microscope (IMA VISTM, Photon Etc.) with a calibrated low-noise silicon CCD camera. A 405 nm continuous-wave (CW) laser was used as a photoexcitation source, and the emission image was re-focused using broadband PL emission from the sample. The spectral measurements are performed by scanning the angle of

the grating relative to the emitted light from the sample to form images at each wavelength which are stacked to form a 3D data cube with x and y as navigation axis and c as wavelength axis.

SEM-CL maps were acquired in an Attolight Allalin 4027 Chronos SEM-CL at room temperature under high vacuum. Beam focusing before each data acquisition was performed away from the sample areas used for the measurements to prevent specimen damage. CL maps were acquired using 5 kV acceleration voltage, 625 pA beam current, and 100 ms/pixel acquisition time. These conditions were found to be the optimum to minimise detrimental beam damage-related effects in the perovskite emission. CL maps were processed and analysed in LumiSpy v.0.1.2[40]. The artefacts caused by cosmic rays saturating the spectrometer were removed, and the edges of each map were cropped out as they tend to show edge effects and higher CL intensities.

The maps of PL intensity and lifetime were obtained using a confocal time-correlated single-photon counting (TCSPC) setup (PicoQuant, MicroTime 200). A 509 nm pulsed laser (2.5 MHz, ~30 fJ) was focused onto the sample with a 100x objective. The emission signal was collected by a TCSPC detector through the same objective. A 20 μm × 20 μm domain was spatially scanned using a Galvano mirror system and confocal pinhole. The lifetime was calculated from the slopes of the initial decay of the transient signal at each pixel.

GIWAXS data was collected at the I07 Surface and Interface Diffraction beamline at the Diamond Light Source (Didcot, UK). The beam energy was 15 keV (0.82656 Å). The scattered beam was collected by a Pilatus 2M large area detector, at a sample-detector distance of 550 mm and calibrated with a lanthanum hexaboride (LaB_6) sample. The incidence angle was kept at 0.3° to achieve bulk-preferential probing with a frame exposure of 1 s. The sample chamber was continuously purged with a 1.5 L min^{-1} He flow. Data was processed with the DAWN software package.

Time-resolved photoluminescence spectroscopy was measured with an electrically gated iCCD camera system (Andor iStar DH740 CCI-010) connected to a grating spectrometer (Andor SR303i). The excitation fluence was estimated as 6 μJ cm^{-2}.

SEM imaging was carried out at high vacuum (< 4×10^{-6} mbar) by a LEO GEMINI 1530VP FEG-SEM system using 20 kV acceleration voltage. The surface morphology was collected by a MFP-3D AFM System (Asylum/Oxford Instruments) in the ambient environment.

Chemical interaction characterisations

FTIR measurements were conducted by using a Fourier transform spectrometer (Nicolet 6700). The system was kept in a nitrogen atmosphere. Samples were prepared by potassium bromide tableting method with background subtraction. XPS spectra were measured by a monochromatic Al $K\alpha_1$ X-ray source using a SPECS PHOIBOS 150 electron energy analyser. ^{127}I NMR measurement was performed on Bruker AVANCE NEO 400 MHz instrument. N, N-Dimethylformamide-d7 was used as solvent to prepare samples for NMR measurement.

Transient Absorption Spectroscopy

All samples were given glass-lid encapsulation. The output of a Ti:sapphire amplifier system (Spectra Physics Solstice Ace) operating at 1 kHz and generating ~100 fs pulses was used as the fundamental laser. The 400-nm pump pulses were created by sending the 800-nm fundamental beam of the Solstice Ace through a second harmonic generating (SHG) beta barium borate (BBO) crystal (Eksma Optics). The broadband white probe was provided by the Disco (Leukos Laser, STM-2-UV) and the pump-probe decay was controlled electronically. The white light was split into two identical beams (probe and reference) by a 50/50 beamsplitter. The reference beam passing through the sample did not interact with the pump, which allows for correcting for any shot-to-shot fluctuations in the probe that would otherwise greatly increase the structured noise in the experiments. Based on this arrangement, small signals with $\Delta T/T \sim 10^{-5}$ could be measured. The transmitted probe and reference pulses were collected with a silicon dual-line array detector (Hamamatsu S8381-1024Q, spectrograph: Andor Shamrock SR-303i-B) driven and read out by a custom-built board (Stresing Entwicklungsbüro).

LED measurement at pulsed mode

Short square voltage pulses were generated by a HP8116A function generator and applied to the device. A 5 Ω resistor was placed in series with the device. Transient voltages were measured using a dual-channel oscilloscope (Agilent Technologies DSO6032A) and the transient current was calculated from the voltage across the resistor in series with the device[41]. A grating spectrometer (Andor SR303i) was used to collect electroluminescence response of the device. Current and light output were averaged over 1500 pulses at each

voltage. The EQE was calibrated by comparing a DC response with that from the standard EQE characterization setup.

DFT simulations

All DFT calculations were done using the Quantum Espresso suite (v7.0). The exchange correlation was approximated by the PBE functional and the core-valence interactions were treated using the ultrasoft pseudopotentials from the GBRV library. The electronic wavefunctions were expanded in a plane wave basis with a cutoff of 40 Ry and charge-density cutoff of 200 Ry, and the dispersion correction was included empirically using the DFT-D3 method. The Brillouin zone of the bulk $FAPbI_3$ perovskite was sampled with a 6 × 6 × 6 Γ-centered Monkhorst-Pack **k**-point grid, the atoms are relaxed until the Hellman-Feynman force converges below 0.01 eV $Å^{-1}$, and the volume until all components of the stress tensor are below 10^{-2} GPa. The passivated and unpassivated perovskite surfaces without defects were created five atomic layers in the *z*-direction, and a vacuum spacing of 20 Å was added to remove any spurious interactions. A commensurate 6 × 6 × 1 **k**-point grid was used to sample the Brillouin zone. For isolated ligands, a vacuum spacing of 20 Å was added in all 3 spatial directions and only the Γ point was sampled.

The binding affinity (E_{bind}) of the ligands to the perovskite surface was computed as

$$E_{bind} = E_{tot} - E_{slab} - E_{ligand}$$

where E_{tot} and E_{slab} are the total energies of the passivated and unpassivated perovskite supercell, respectively, and E_{ligand} is the energy of the isolated ligand.

Photothermal deflection spectroscopy

Photothermal deflection spectroscopy measurements were performed in the transverse configuration, utilising a probe beam from a 670 nm diode laser and a pump beam from a tuneable light source consisting of a 250 W quartz tungsten halogen lamp and a 250 mm focal length grating monochromator. The pump beam was mechanically chopped at 10 Hz and passed to a vibration-isolated optical table through a fibre. The light-induced local heating of the sample changing periodically the optical path of the probe beam was quantitatively analysed with a quadrant Si photodiode, with the generated signal proportional to the material absorbance demodulated with a lock-in amplifier (Stanford Research Systems SR830). The perovskite samples, spin-coated on fused silica substrates (Spectrosil 2000), were immersed in 3M Fluorinert FC-72 as the thermooptic medium. For ZnO nanoparticles dispersed in

isopropyl alcohol, the measurement was done *in situ* by passing the probe beam through a solution-filled quartz cuvette, with isopropyl alcohol serving as the medium.

Method References

35. Wang, J. *et al.* Interfacial Control Toward Efficient and Low-Voltage Perovskite Light-Emitting Diodes. *Adv. Mater.* **27**, 2311–2316 (2015).

36. Hu, J. *et al.* Aryl-perfluoroaryl interaction in two-dimensional organic–inorganic hybrid perovskites boosts Stability and photovoltaic efficiency. *Acs. Mater. Lett.* **1**, 171–176 (2019).

37. Di, D. *et al.* High-performance light-emitting diodes based on carbene-metal-amides. *Science* **356**, 159–163 (2017).

38. Kim, J. S. et al. Ultra-bright, efficient and stable perovskite light-emitting diodes. Nature **611**, 688–694 (2022).

39. Mello, J. C. de, Wittmann, H. F. & Friend, R. H. An improved experimental determination of external photoluminescence quantum efficiency. *Adv. Mater.* **9**, 230–232 (1997).

40. Orri, J. F., Lähnemann, J., Prestat, E., Johnstone, D. N. & Tappy, N. LumiSpy/lumispy: Release v0.1.2. *Zenodo* (2021).

41. Cho, C. *et al.* Electrical pumping of perovskite diodes: toward stimulated emission. *Adv. Sci.* **8**, 2101663 (2021).

Data Availability

The data underlying this paper are available at the University of Cambridge repository (https://doi.org/10.17863/CAM.92711).

Code Availability

Not applicable.

Competing interests

The authors declare no competing interests.

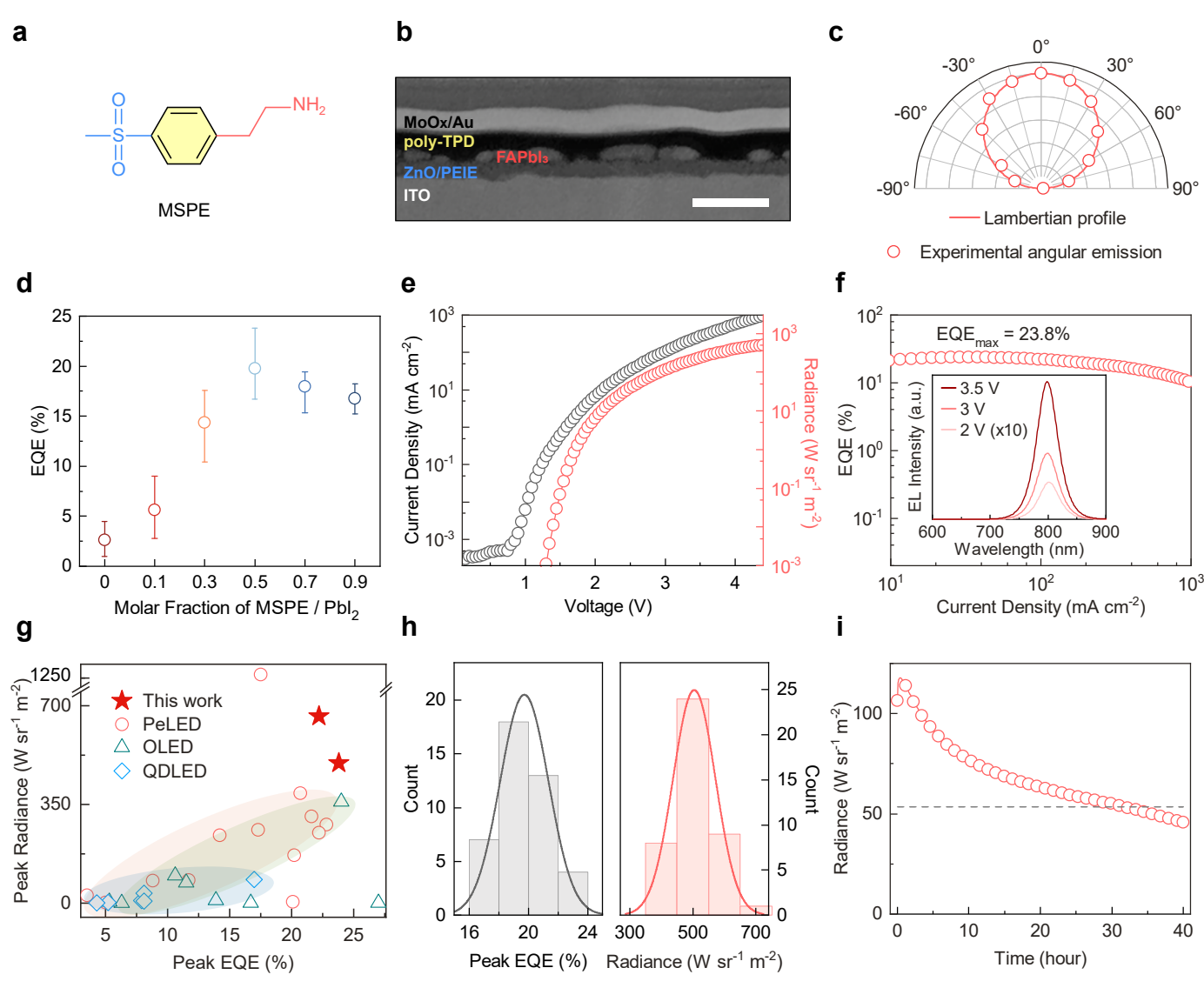
a
NH2
MSPE
b
MoOx/Au
poly-TPD
FAPbI3
ZnO/PEIE
ITO
c
0°
-30°
30°
-60°
60°
-90°
90°
Lambertian profile
Experimental angular emission
d
EQE (%)
Molar Fraction of MSPE / PbI2
e
Current Density (mA cm-2)
Radiance (W sr-1 m-2)
Voltage (V)
f
EQEmax = 23.8%
EQE (%)
3.5 V
3 V
2 V (x10)
EL Intensity (a.u.)
Wavelength (nm)
Current Density (mA cm-2)
g
This work
PeLED
OLED
QDLED
Peak Radiance (W sr-1 m-2)
Peak EQE (%)
h
Count
Peak EQE (%)
Radiance (W sr-1 m-2)
i
Radiance (W sr-1 m-2)
Time (hour)

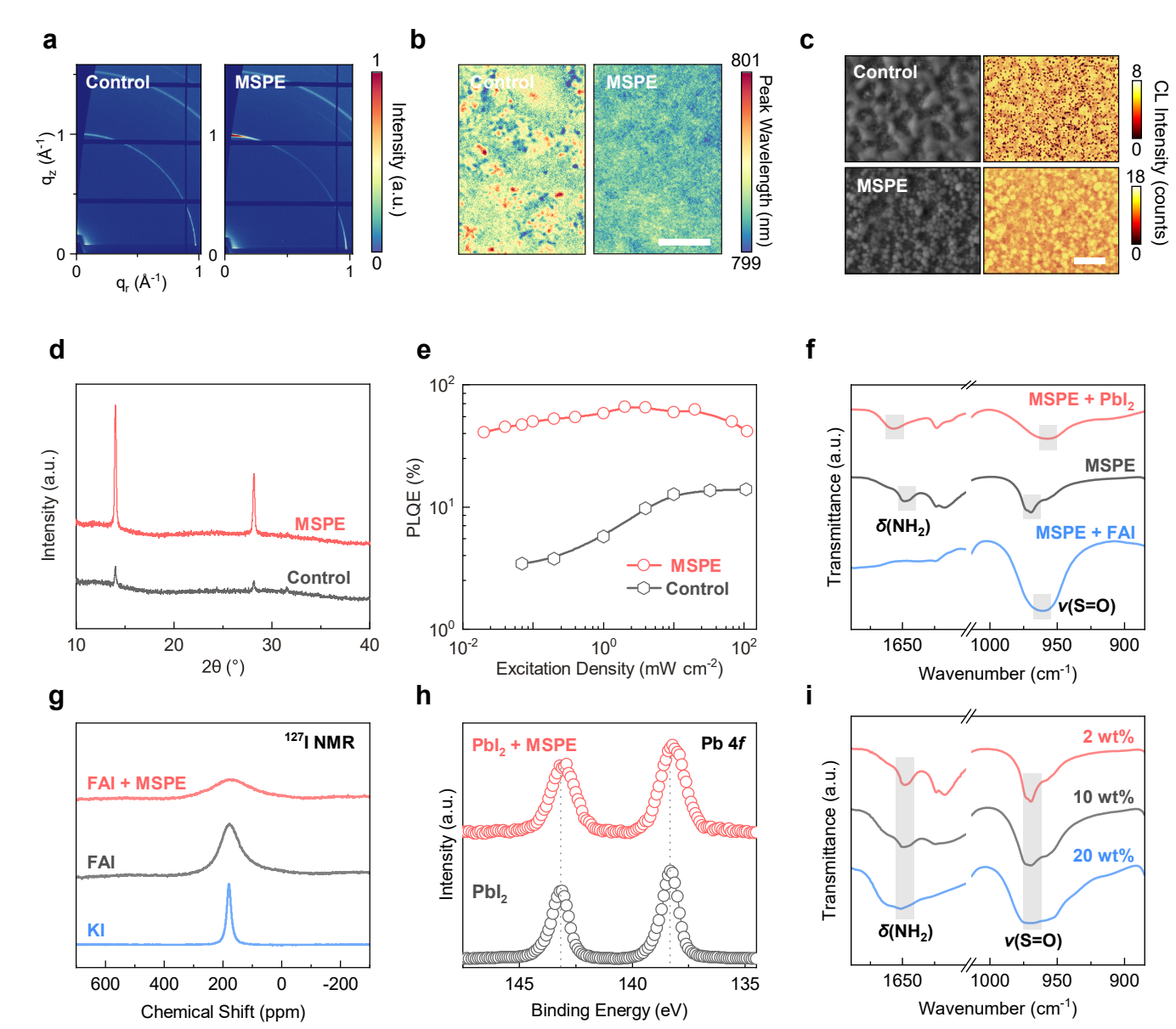
a
Control
MSPE
q_z (Å^{-1})
q_r (Å^{-1})
Intensity (a.u.)
b
Control
MSPE
Peak Wavelength (nm)
801
799
c
Control
MSPE
CL Intensity (counts)
d
MSPE
Control
Intensity (a.u.)
2θ (°)
e
MSPE
Control
PLQE (%)
Excitation Density (mW cm^{-2})
f
MSPE + PbI$_2$
MSPE
MSPE + FAI
δ(NH$_2$)
ν(S=O)
Transmittance (a.u.)
Wavenumber (cm^{-1})
g
^{127}I NMR
FAI + MSPE
FAI
KI
Chemical Shift (ppm)
h
PbI$_2$ + MSPE
Pb 4f
PbI$_2$
Intensity (a.u.)
Binding Energy (eV)
i
2 wt%
10 wt%
20 wt%
δ(NH$_2$)
ν(S=O)
Transmittance (a.u.)
Wavenumber (cm^{-1})

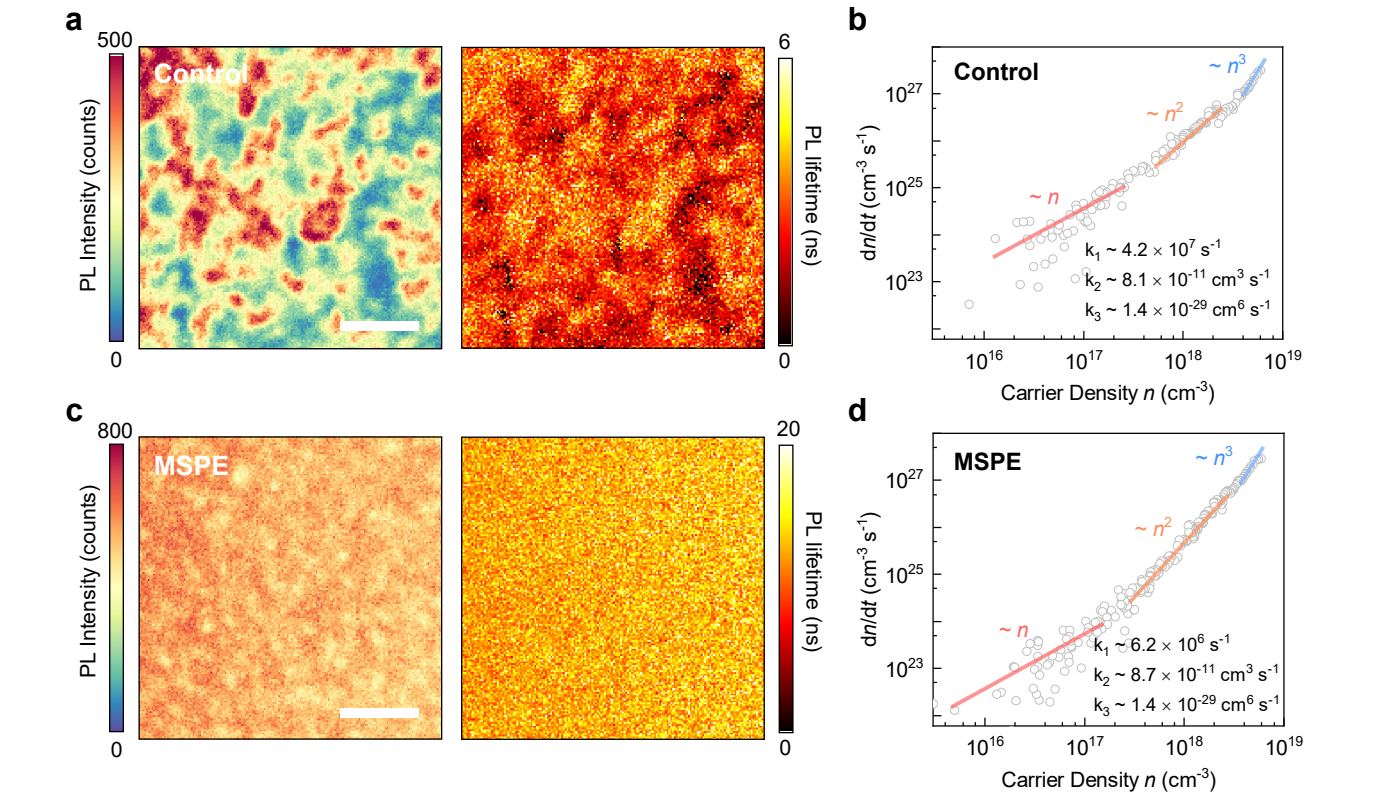
a
500
Control
PL Intensity (counts)
0
6
PL lifetime (ns)
0
b
Control
~ n^3
~ n^2
~ n
k_1 ~ 4.2 × 10^7 s^{-1}
k_2 ~ 8.1 × 10^{-11} cm^3 s^{-1}
k_3 ~ 1.4 × 10^{-29} cm^6 s^{-1}
10^{27}
10^{25}
10^{23}
dn/dt (cm^{-3} s^{-1})
10^{16}
10^{17}
10^{18}
10^{19}
Carrier Density n (cm^{-3})
c
800
MSPE
PL Intensity (counts)
0
20
PL lifetime (ns)
0
d
MSPE
~ n^3
~ n^2
~ n
k_1 ~ 6.2 × 10^6 s^{-1}
k_2 ~ 8.7 × 10^{-11} cm^3 s^{-1}
k_3 ~ 1.4 × 10^{-29} cm^6 s^{-1}
10^{27}
10^{25}
10^{23}
dn/dt (cm^{-3} s^{-1})
10^{16}
10^{17}
10^{18}
10^{19}
Carrier Density n (cm^{-3})

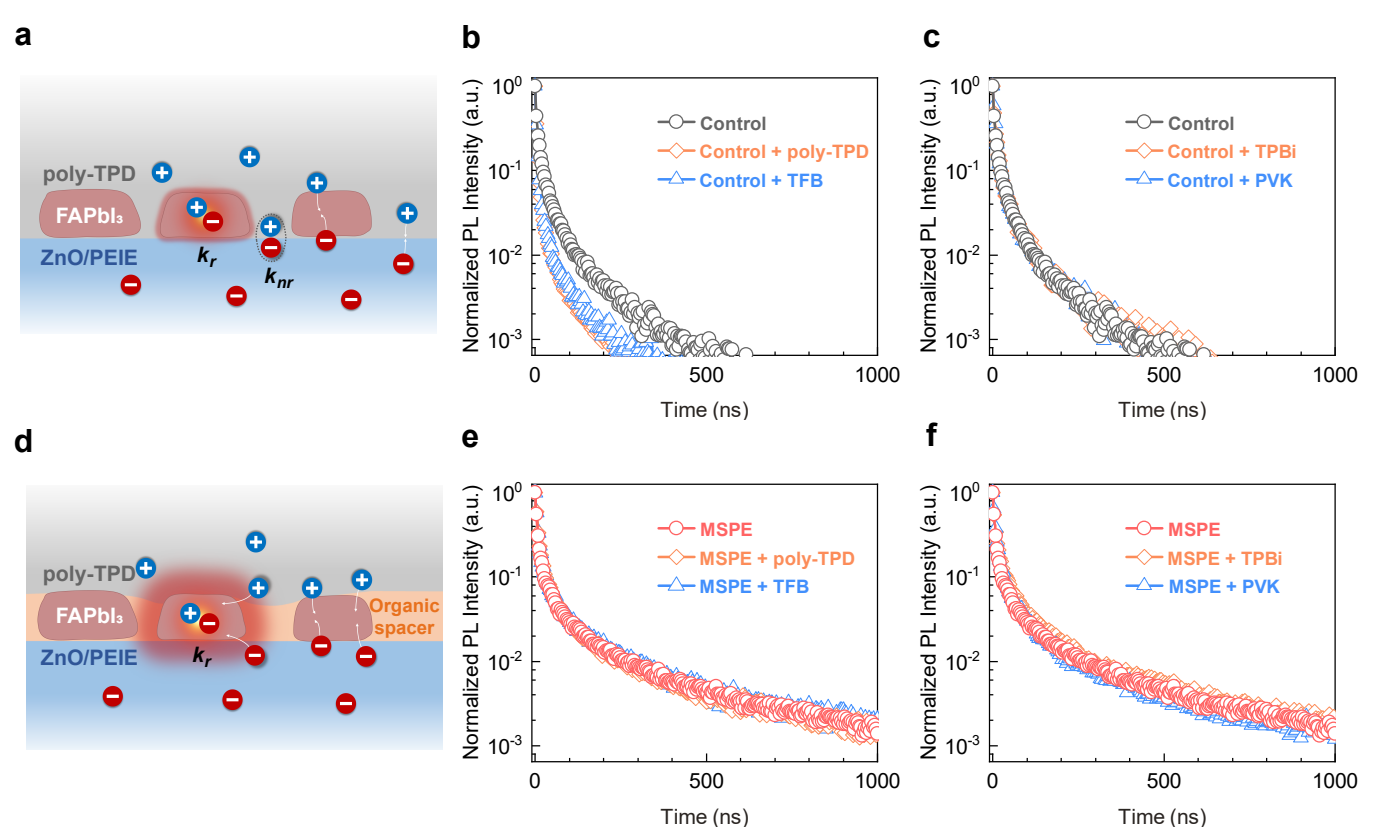
a
poly-TPD
FAPbI3
ZnO/PEIE
kr
knr
b
Normalized PL Intensity (a.u.)
Time (ns)
Control
Control + poly-TPD
Control + TFB
c
Control
Control + TPBi
Control + PVK
d
poly-TPD
FAPbI3
ZnO/PEIE
kr
Organic spacer
e
MSPE
MSPE + poly-TPD
MSPE + TFB
f
MSPE
MSPE + TPBi
MSPE + PVK